THE JOURNAL OF PHYSICAL CHEMISTRY C
A JOURNAL OF THE AMERICAN CHEMICAL SOCIETY

pubs.acs.org/JPCC
Article

Monte Carlo Simulations of Water Adsorption in Aluminum Oxide Rod-Based Metal−Organic Frameworks

Saumil Chheda, WooSeok Jeong, Nikita Hanikel, Laura Gagliardi,* and J. Ilja Siepmann*

Cite This: J. Phys. Chem. C 2023, 127, 7837−7851
Read Online

ACCESS | Metrics & More | Article Recommendations | Supporting Information

ABSTRACT: Atmospheric water harvesting utilizing nanoporous sorbent materials with suitable adsorption characteristics has recently emerged as a potential solution for the global water crisis. Here, we probe the adsorption behavior of two high-performing Al(μ_2-OH) rod-based metal−organic frameworks (MOFs), MOF-303 and MOF-333, using Gibbs ensemble Monte Carlo simulations. We find that simulations using nonpolarizable force fields and rigid framework structures optimized using periodic electronic structure calculations can achieve good agreement with experimental data for adsorption isotherms and isosteric heats of adsorption; however, for MOF-303, it is important to utilize a structure that accounts for the distortion associated with water adsorbed at the primary adsorption site.

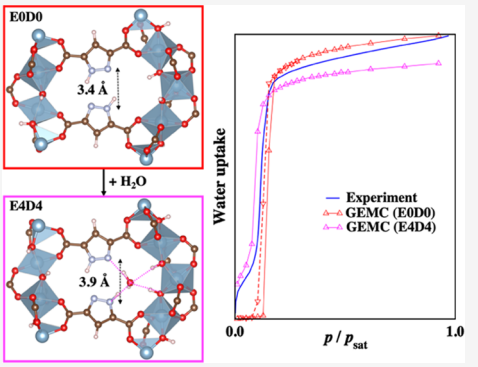

INTRODUCTION

Atmospheric water harvesting (AWH) has gained increasing attention as a potential solution for the rising global water crisis.[1−6] An AWH device operates in a two-step cycle. In the first step, water vapor is directly captured from the atmosphere through adsorption into a nanoporous sorbent material. During the second step, the sorbent is thermally regenerated, thus resulting in the release of the adsorbed water as concentrated water vapor, which can be easily condensed and collected. A high-performing AWH sorbent must offer adsorption sites with sufficient affinity to capture water at the desired humidity level but not bind the water molecules too tightly to allow for energy-efficient regeneration. Metal−organic frameworks (MOFs) offer exciting opportunities for AWH owing to their highly tunable water adsorption characteristics that can range from extremely hydrophilic sorbents, such as aluminosilicates, to hydrophobic sorbents, comparable to all-silica zeolites and nonpolar polymer gels.[7−9]

MOF-303 is a state-of-the-art sorbent for AWH devices that was able to deliver 0.7 L kg^{-1} day^{-1} upon rapid cycling in the arid conditions of the Mojave desert (conditions as extreme as 10% RH (relative humidity) and 27 °C).[4] MOF-303 [Al(μ_2-OH)(PZDC)] is constituted from infinite (in the sense of extending through an entire crystallographic domain) inorganic Al(μ_2-OH) rods, formed from alternating *cis*−*trans* corner-sharing $AlO_4(\mu_2\text{-}OH)_2$ connected by 1-*H*-pyrazole-3,5-dicarboxylate (PZDC) linkers that encompass hydrophilic one-dimensional (1-D) channels with an approximately square cross section (Figure 1A). These channels can fit a sphere with a diameter of about 6 Å. Recently, using a combination of single-crystal X-ray diffraction (SCXRD) experiments and periodic density functional theory (DFT) calculations, we identified the water adsorption sites and the molecule-by-molecule water uptake mechanism in MOF-303.[6] The alternating orientation of the PZDC linkers leads to patches on the pore wall with different degrees of hydrophilicity found in each of the four asymmetric units contained in the crystallographic cell (Figure 1B). The primary adsorption site for the initial uptake of one water molecule per asymmetric unit is situated on the more hydrophilic patch and allows for the formation of hydrogen bonds with the pyrazole functionalities ($N(H)_{linker}$, N_{linker}) and one of the two bridging μ_2-OH groups (O_{rod}) ($r_{O_{wat}-X_{framework}}$ values range from 2.7 to 3.0 Å, where $X_{framework}$ = N_{linker}, $N(H)_{linker}$, or O_{rod}) that results in a binding energy of about −80 to −90 kJ mol^{-1} (Figure 1C). The binding of water in the primary site is accompanied by a distortion of the linker orientations that increases the distances, $r_{NH\text{-}N}$, between opposite pyrazole functionalities on the hydrophilic surface patch by about 0.4 Å. Due to the high adsorption strength of this primary site, regeneration of MOF-303 during the thermal desorption step is not complete at mild temperatures.[6] Insights into the role of the linkers in forming the primary adsorption site were used to design an isoreticular MOF analogue, MOF-333, in which the PZDC linkers are replaced by 2,4-furandicarboxylate (FDC) linkers,[6] thus leading to a reduction in the binding energy for the

Received: January 16, 2023
Revised: March 18, 2023
Published: April 16, 2023

https://doi.org/10.1021/acs.jpcc.3c00354
J. Phys. Chem. C 2023, 127, 7837−7851

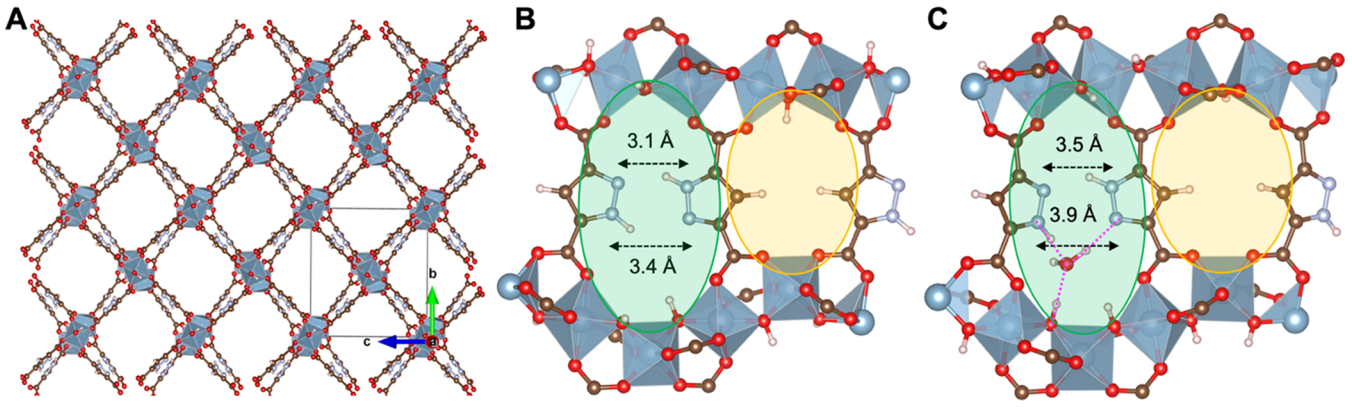

Figure 1. (A) MOF-303 is formed from infinite Al(μ_2-OH) rods aligned with the crystallographic *a*-axis that are connected by PZDC linkers. The image shows a 3 × 2 × 3 supercell of MOF-303 as used in the simulations. (B) Illustration of the pore walls for an asymmetric unit (for clarity, some of the surrounding atoms are shown) of the pristine MOF-303 structure.[6] The linker arrangement with the polar parts (N-NH) of two PZDC linkers pointing toward each other and their neighboring μ_2-OH groups leads to the formation of one strongly hydrophilic surface region (SH region shaded in green), whereas the surface region with the two CH groups of the PZDC linkers pointing toward each other is less hydrophilic (LH region shaded in yellow). The distances, $r_{NH\text{-}N}$, between opposite pyrazole functionalities are indicated. (C) Illustration of the primary adsorption site (located in the SH region) for water in MOF-303 through hydrogen-bond formation with neighboring $N(H)_{linker}$, N_{linker}, and O_{rod} functionalities (pink dotted lines) determined from SCXRD measurements[6] and periodic DFT calculations (E0D0 and E4D4 structures, see below). Color code: Al, blue octahedra; O, red; N, light blue; C, brown; and H, light pink.

initial water molecules to about −60 kJ mol^{-1}. This reduction allows for nearly complete water release during the desorption step and an increase of the productivity of the AWH device.

While water binding energies computed using DFT or with wave function theory[10] allow one to gauge the adsorption strength of different binding sites in a given MOF, it is difficult to quantitatively predict the water loading of the MOF as a function of RH and temperature using these computed binding energies when water−water interactions also play an important role. First-principles Monte Carlo (FPMC) simulations of adsorption isotherms[11,12] are computationally extremely demanding and, relevant for AWH applications, suffer from the shortcoming that converting pressure to RH is ambiguous because the saturated vapor pressure of water near room temperature for a given DFT model is not known.[13]

Force-field-based Monte Carlo simulations greatly reduce the computational demand compared to the FPMC simulations, and can be used to predict the water adsorption isotherms in MOFs and other adsorbents.[14−21] While generalized force fields, such as UFF[22] and DREIDING,[23] are commonly used to describe MOF−adsorbate interactions and work well for nonpolar adsorbate molecules, such as alkanes, these force fields can fail to accurately predict the uptake of polar guest molecules that can form hydrogen bonds with the MOF.[24] In many studies employing these generalized force fields, the presence of structural defects in the MOF is suggested to enhance the hydrophilicity of the framework and to yield better agreement with experimental adsorption isotherms.[24,25] Another problem encountered for molecular simulation of water adsorption is that widely used water models (e.g., SPC/E,[26] TIP4P,[27] and TIP4P/2005[28]) yield rather different saturated vapor pressures at a given temperature, which in turn makes it difficult to compare to the experimental water uptake pressures. Moreover, grand canonical Monte Carlo simulations rely on an equation of state to relate the chemical potential of the sorbate compound to its pressure in the vapor phase,[29] and an equation of state representing the experimental behavior of water may not be suitable for a given water model.

Here, we performed isobaric−isothermal (*NpT*) Gibbs ensemble Monte Carlo (GEMC)[30,31] simulations to predict the water adsorption properties in MOF-303 and its isoreticular analogue, MOF-333, at T = 298 K. In *NpT*-GEMC simulations, the (gas-phase) reservoir is simulated explicitly (i.e., accounting for intermolecular interactions) and, hence, an equation of state is not needed. For applications that consider the adsorption behavior close to the saturated vapor pressure, p_{sat}, of the adsorbate molecules, it is important to obtain p_{sat} for the chosen molecular model through separate GEMC simulations so that adsorption isotherms can be shown as a function of relative pressure (i.e., p/p_{sat} or RH). With the knowledge obtained from SCXRD[6] that water adsorption leads to opening of the primary adsorption sites (Figure 1) and also to slight changes in the unit cell parameters of MOF-303, we explored five different structural variants of MOF-303 for the GEMC simulations: E0D0, E0D4, E4D4, E4E4, and D4D4 (Table S1). The first letter and number denote the source of the unit cell parameters (i.e., E0 and E4 stand for the experimental unit cells of pristine MOF-303 without water molecules and MOF-303 with four water molecules per unit cell, respectively, and D4 denotes lattice parameters obtained from a full DFT optimization in the presence of four water molecules per unit cell). The second letter and number denote the choice for the location of the framework atoms (i.e., D0, D4, and E4 denote atomic positions resulting from DFT optimization with zero and four water molecules per unit cell and the experimental coordinates with no optimization, respectively). Although the choice of using E*x*D*y* structures may at first glance appear surprising, this choice reflects that unit cell parameters reported from the experimental SCXRD values are directly obtained from the reflection positions and are the gold standard for the lattice parameters, whereas the determination of the atomic position from SCXRD requires data processing that comes with some uncertainty, and DFT optimization constrained by the experimental lattice parameters can potentially refine the atomic positions. Details of the DFT optimization are provided in the Computational Methods section. The water molecules were represented by the TIP4P model[27] for most systems because this model yields a

https://doi.org/10.1021/acs.jpcc.3c00354
J. Phys. Chem. C 2023, 127, 7837−7851

more accurate saturated vapor pressure near 300 K than other models[32] and yields more accurate predictions of fluid phase equilibria with nonpolar molecules.[33] The MOF linkers are represented by the TraPPE-EH (transferable potentials for phase equilibria-explicit hydrogen) model that is parameterized using phase equilibrium data,[34] while three force-field variants were considered for the inorganic Al(μ_2-OH) units.

COMPUTATIONAL METHODS

Periodic DFT Optimization. The atomic coordinates from different experimental crystal structures of MOFs (MOF-303 and MOF-333) with different water loadings were used as starting points for geometry optimizations using the plane-wave density functional theory (DFT) method in the Vienna Ab Initio Simulation Package (VASP; version 6.2).[35−37] A single unit cell of the MOF [Al(μ_2-OH)(PZDC or FDC)]$_8$ without or in the presence of a specific number of adsorbed water molecules was used for all geometry optimizations. The lattice cell of the MOF structure was not changed during the optimizations unless noted otherwise. The optimizations were performed using the Perdew−Burke−Ernzerhof (PBE) exchange−correlation density functional along with Grimme's D3 dispersion corrections with Becke−Johnson damping.[38,39] A plane-wave basis set with an energy cutoff of 520 eV was used for all optimizations. The structures were optimized until the electronic energies and forces on the atoms converged within 10^{-6} eV and 0.02 eV Å^{-1} respectively. The lattice energies of the optimized structures were obtained from single-point energy calculations using a higher energy cutoff of 850 eV. For the single-point energy calculations, energy and force convergence criteria of 10^{-8} eV and 0.01 eV Å^{-1} were used.

Second-Order Møller−Plesset (MP2) Perturbation Theory Calculations. The binding energies of water molecules adsorbed in the primary site were also computed using the MP2 theory[40,41] implemented in the Gaussian 16 (Revision C.01) software[42] as a benchmark for comparing the water binding energies computed using different force fields. Representative cluster models encompassing the primary site for water adsorption were extracted from the DFT-optimized unit cells of the respective MOFs and were used for MP2 calculations. Each cluster model included two opposite-facing PZDC linkers (MOF-303) or FDC linkers (MOF-333), three AlO$_4$(μ_2-OH)$_2$ octahedra of the inorganic rod connecting the two linkers on the wider side of the patch, and a water molecule adsorbed in the primary site in case of the water-loaded structures. The narrower side of the region and the Al(μ_2-OH) rods were truncated with Li^+ ions to maintain the overall charge neutrality of the model. The remaining linkers connected to the AlO$_4$(μ_2-OH)$_2$ octahedra were truncated as formate groups. The positions of the Li^+ ions and the H atom of the formate groups were first optimized using DFT (PBE-D3 exchange−correlation functional and cc-pVTZ[43,44] basis sets for all atoms), while spatially freezing the positions of the other framework atoms extracted from the DFT-optimized unit cell. Single-point energy calculations were then performed on the optimized cluster models using the MP2 method and cc-pVDZ basis set for all atoms to compute the water binding energies. For reference, the energy of an isolated water molecule was also obtained at the same level of theory.

Gibbs Ensemble Monte Carlo (GEMC) Simulations. Force-field-based Monte Carlo (MC) simulations were performed in the isobaric−isothermal (NpT) Gibbs ensemble[30,31] to study the water adsorption in MOFs using the Monte Carlo for Complex Chemical Systems-MN software (MCCCS-MN).[45] The vapor-phase unary adsorption of water in the MOFs was studied using two simulation boxes (sorbent phase and water reservoir) held in a thermodynamic contact. A 3 × 2 × 3 supercell of the MOF, obtained from either the experimental or the DFT-optimized crystal structure, was used as the sorbent and kept rigid throughout the simulations. In each adsorption simulation, rigid-body translational and rotational moves were performed on randomly selected water molecules. Swap moves allowed for the transfer of water molecules between the two simulation boxes (first randomly selecting the transfer direction and then one of the available water molecules). Volume moves were performed only on the reservoir box to allow it to maintain the target pressure upon transfer of water molecules to the sorbent box. The Monte Carlo moves were randomly distributed between volume, swap, translational, and rotational moves in the ratio of 0.01:0.39:0.30:0.30.

The adsorption/desorption simulations were performed using N = 1000 water molecules at T = 298 K and p/p_{sat} (or relative humidity, RH) = 0.01−1.0, where p_{sat} is the saturated vapor pressure of the water model. Simulations for the adsorption branch were started using an empty MOF box without preadsorbed water molecules (even if water molecules were present during the DFT optimization of the water-loaded MOF structures); and those for the desorption branch were started from water-saturated MOF structures (about 600 water molecules in the supercell). Each simulation was equilibrated for at least 1 × 10^5 MC cycles (where 1 MC cycle consists of N MC moves) followed by at least another 2 × 10^5 MC cycles for the production period. The production period was divided into eight equal blocks to determine the statistical uncertainties in the adsorbed water loading at each target pressure.

The interactions of water molecules with the framework were described using various force fields. The nonbonded Lennard-Jones (LJ) interaction parameters for the Al and O atoms of the inorganic rods comprising Al(μ_2-OH) units were taken from the UFF force field,[22] while three different sets of LJ parameters were considered for the H atom of the Al(μ_2-OH) unit: UFF,[22] DREIDING,[23] and no LJ interactions (i.e., ε/k_B = 0.0 K). The LJ interaction parameters for the linkers were taken from the TraPPE force field.[34] The partial charges of the inorganic Al(μ_2-OH) units of the rods were obtained from the DDEC6 charge scheme,[46] while the partial charges for the aromatic rings of the linkers were taken as given in the TraPPE force field for the respective aromatic molecules. The partial charges of the carboxylate groups were then adjusted starting from the DDEC partial charges to maintain the overall neutrality of the framework (see Tables S3 and S11 for the list of the force-field parameters). The intermolecular interactions of water molecules were described using the TIP4P water model[27] (p_{sat} = 4.54 ± 0.12 kPa at T = 298 K) for all MOF structures, while the TIP4P/2005[28] water model (p_{sat} = 0.739 ± 0.017 kPa at T = 298 K)[47] was also tested for one MOF structure. (For comparison, the experimental vapor pressure at T = 298 K is 3.139 kPa.[48]) Both these models represent a water molecule as a rigid particle with four interaction sites including an extra charge site placed on the H−O−H bisector. Since the framework was kept rigid during the adsorption simulations, only the MOF−water and water−water interactions were included. The Lorentz−Berthelot mixing rules were used to describe these MOF−water LJ interactions. A spherical cutoff of 14 Å was used for truncating the pairwise Lennard-Jones and Coulomb interactions. Analytical tail corrections for the LJ interactions and the

https://doi.org/10.1021/acs.jpcc.3c00354
J. Phys. Chem. C 2023, 127, 7837−7851

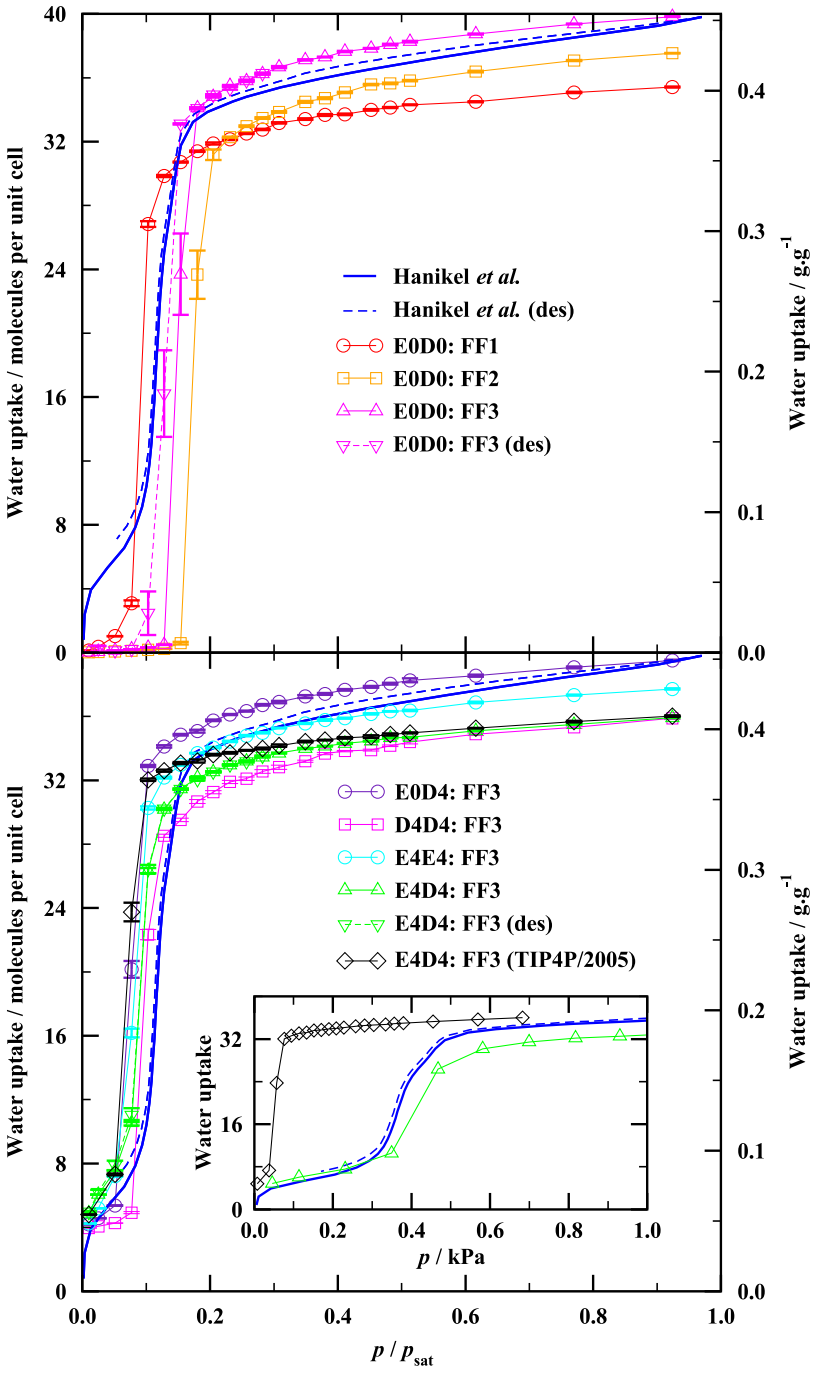

Figure 2. Comparison of the simulated water sorption isotherms at $T = 298$ K for the different MOF-303 structural variants to the experimental data by Hanikel et al.[6] Unless otherwise noted, simulations were carried out with the TIP4P water model, and only the adsorption branch is shown. (Top) Comparison showing the effects of varying the Lennard-Jones parameter used for the hydrogen atom of the Al(μ_2-OH) units in the pristine MOF-303 structure optimized in the absence of adsorbed water molecules (D0) but using the experimental lattice parameters (E0). (Bottom) Comparisons showing the influence of the choice of lattice parameters for DFT optimization with four water molecules per unit cell occupying the primary adsorption sites and between TIP4P and TIP4P/2005 water models (inset shows loading as a function of absolute pressure).

Ewald summation method for electrostatic interactions were employed.

The isosteric heat of water adsorption, defined as the difference in the excess partial molar enthalpy of the adsorbate in the adsorbed phase and its partial molar enthalpy in the bulk phase,[49] was computed from the fluctuations in the potential energy of the adsorbed phase and adsorbed water loading using eq 1

$$-Q_{st} = \frac{\langle U_a N_a \rangle - \langle U_a \rangle \langle N_a \rangle}{\langle N_a^2 \rangle - \langle N_a \rangle^2} - \frac{\langle U_g \rangle + p\langle V_g \rangle}{\langle N_g \rangle} \quad (1)$$

where U_a is the potential energy of the adsorbed phase comprising adsorbate-adsorbate and adsorbate−framework interactions, and N_a is the number of adsorbed molecules in the MOF. Similarly, U_g and N_g are the potential energy and number of adsorbate molecules in the reservoir phase, respectively. It should be noted that the kinetic energy per

https://doi.org/10.1021/acs.jpcc.3c00354
J. Phys. Chem. C 2023, 127, 7837−7851

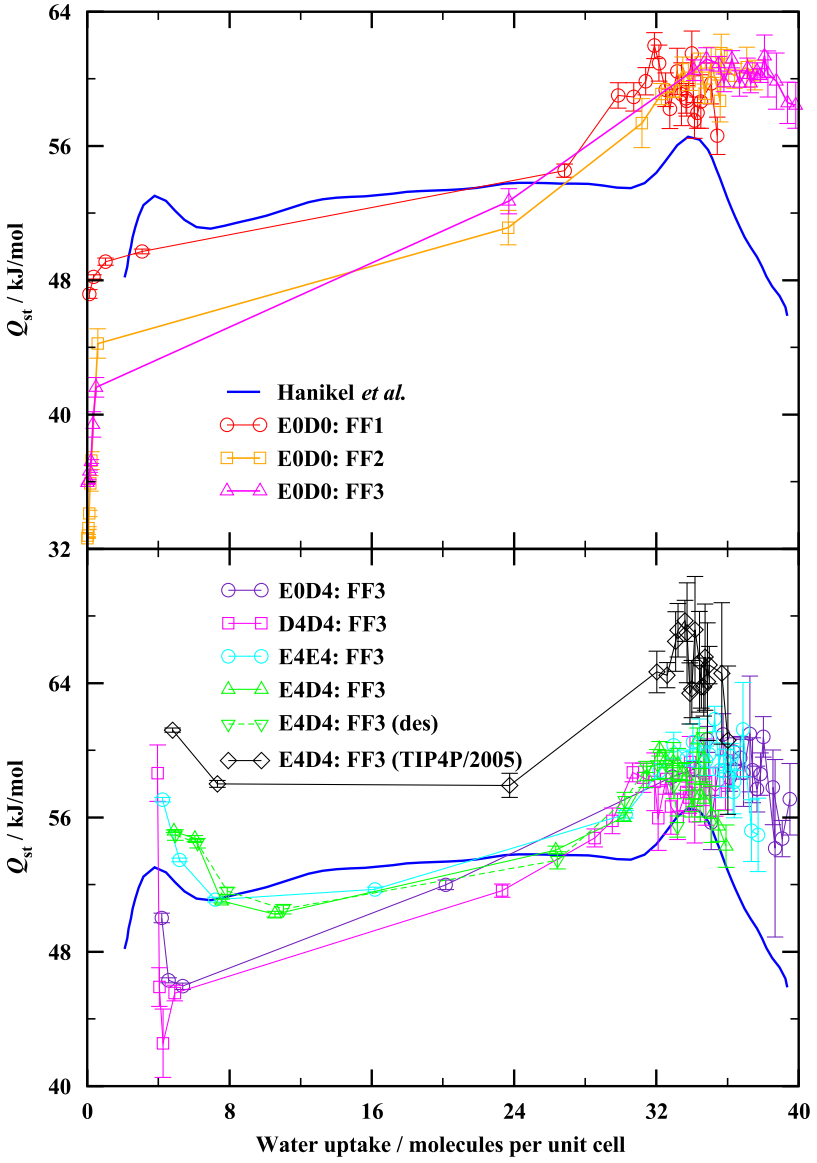

Figure 3. Comparison of isosteric heat of adsorption at T = 298 K in different MOF-303 structural variants to the experimental data by Hanikel et al.[6] (estimated from data at multiple temperatures using the Clausius−Clapeyron equation). Unless otherwise noted, simulations were carried out with the TIP4P water model, and only data for the adsorption branch is shown. (Top) Comparison showing the effects of variations in the Lennard-Jones parameter used for the hydrogen atom of the Al(μ_2-OH) units in pristine MOF-303 structure optimized in the absence of adsorbed water molecules (D0) but using the experimental lattice parameters (E0). (Bottom) Comparisons showing the influence of the choice of lattice parameters for the DFT optimization with four water molecules occupying the primary adsorption sites and between TIP4P and TIP4P/2005 water models.

water molecule is not sampled in the GEMC simulations (i.e., it corresponds to the ensemble average obtained from integration over the momenta) and, hence, does not need to be included in the fluctuation formula.

RESULTS AND DISCUSSION

Adsorption in MOF-303. Preliminary simulations indicated that the water uptake in the primary adsorption site is very sensitive to the interaction parameters used for the hydrogen atom belonging to the Al(μ_2-OH) units that form one hydrogen bond per water molecule (Figure 1C). Thus, three different choices for the Lennard-Jones (LJ) interaction parameters were explored (Table S3): FF1 with σ = 2.571 Å and ε/k_B = 22.14 K from the UFF force field,[22] FF2 with σ = 2.846 Å and ε/k_B = 0.05 K from the DREIDING force field,[23] and FF3 with no LJ interactions as used for hydroxyl groups in the TraPPE force field[50,51] and also in the TIP4P water model. The $O_{acceptor}\cdots H$ distance corresponding to a hydrogen bond is about 1.8 Å and falls deeply within the repulsive region for the FF1 and FF2 models (Table S4). The problem that different LJ parameters are needed for a polar hydrogen atom (connected to either an oxygen or nitrogen atom) than a nonpolar hydrogen atom (connected to a carbon atom) or a less polar hydrogen atom (e.g., hydrogen sulfide) is well known from force fields developed for organic molecules.[52,53] Similarly, Wardzala et al. reported that the diffusion of acetone in a Zr-based MOF, UiO-66, is better described when no LJ site is placed on the H atom of the hydroxyl groups because the UFF force field does not allow these H atoms to act as hydrogen-bond donors.[54]

For MOF-303, the large LJ size parameters for FF1 and FF2 strongly affect the binding energy in the primary site and shift the water molecule away from the hydrogen atoms of the Al(μ_2-

https://doi.org/10.1021/acs.jpcc.3c00354
J. Phys. Chem. C 2023, 127, 7837−7851

OH) rods. Binding energies computed for the DFT (PBE-D3) optimized geometries deviate from the DFT binding energies for the E4D4 and D4D4 structures by +220 and +410 kJ mol^{-1}, respectively, for FF1 and by +11 and +44 kJ mol^{-1}, respectively, for FF2 (Table S5). In contrast, the deviations for FF3 are only −9 and +10 kJ mol^{-1}, respectively. Although not as pronounced, calculations of the binding energies at the optimal FF geometries (i.e., the water molecules are allowed to relax in the field of the rigid MOF structure) yield average deviations of +27, +19, and −6 kJ mol^{-1} for FF1, FF2, and FF3, respectively, compared to their DFT counterparts (Table S5). Calculations using second-order Møller−Plesset (MP2) theory for a cluster model comprising the primary water adsorption site yield energies that are more favorable (larger in magnitude) by 9 and 27 mol^{-1} for the E4D4 and D4D4 structures than the PBE-D3 calculations (Table S5). Considering the MP2 calculations as the benchmark, the average deviations become +46, +38, and +12 kJ mol^{-1} for FF1, FF2, and FF3, respectively. Thus, the FF3 model yields binding energies that fall in between the PBE-D3 and MP2 values, whereas FF1 and FF2 result in significantly weaker binding of water molecules at the primary site. It should be noted that the binding energies for the electronic structure calculations explicitly include the energetic penalty for the distortion of the framework atoms upon adsorption of the water molecules in the primary site. Here, we need to emphasize that we do not intend to tune the force field for the MOF by fitting to any electronic structure calculations; we only use these data to support the selection of the likely best parameter set among three popular options to describe the initial water uptake (Henry's law region) in the primary site that occurs at very low RH < 2%. The primary sites are not involved in the steep step of the adsorption isotherm that governs the performance in an AWH device.

The water adsorption isotherms computed for the DFT-optimized pristine MOF-303 structure (E0D0) using the FF1, FF2, and FF3 parameters and TIP4P water model are shown in Figure 2 (numerical data for the simulated isotherms in all MOF-303 structural variants are reported in Table S6). As expected, the saturation loadings predicted by these models vary inversely with the strength of the repulsive interactions for water molecules with the H_{rod} atoms, i.e., FF3 predicts the highest saturated water loading followed by FF2 and FF1. The location of the step in the adsorption isotherm is also influenced by the H_{rod} parameters. Likely due to the large value of the well depth for H_{rod} atoms (allowing for more favorable dispersion interactions), the inflection point for the step is shifted most to the low RH for FF1 compared to FF2 and FF3. An additional factor contributing to the shift to lower RH may be that the large size of the LJ diameter for FF1 leads to an effectively smaller pore diameter. The well depth for FF2 (ε/k_B = 0.05 K) is too small to affect the water interactions away from the primary site, but it weakens the water interactions with all hydrogen atoms of the Al(μ_2-OH) rods and, hence, the more hydrophobic walls yield an inflection point shifted to higher RH than for FF3.

More importantly, the isotherms obtained for the pristine MOF-303 structure do not yield the initial uptake of four water molecules per unit cell at RH < 3% associated with the strong interactions with the primary site and underestimate the magnitude of the heat of adsorption, Q_{st}, by about 10 kJ mol^{-1} (Figure 3). For the FF3 model at RH = 13% before the condensation step, we find only 0.5 water molecules per unit cell. Of those, only 0.07 water molecules occupy the primary site (about 20% of the water molecules adsorbed at this condition), and the remaining water molecules are distributed over numerous sites (Figure S3 and Table S7). The increase in Q_{st} observed for FF3 in the E0D0 structure as the loading increases from 0.1 to 0.5 water molecules per unit cell is associated with water−water interactions. As indicated in Figure 1, adsorption at the primary site is associated with formation of a "pocket" by increasing the distance between opposite pyrazole functionalities (allowing the water molecule to move closer to the plane of the PZDC linkers).[6] Given the structural change occurring when the first water molecules are adsorbed, we anticipate that MOF-303 structural variants including this pocket may allow for a better representation of the adsorption isotherm. Thus, we now shift our discussion to adsorption isotherms obtained for such structures and present data only for the FF3 parameters that yield the best agreement with the binding energy and structure determined from electronic structure calculations (Table S5, isotherms simulated for the other force fields are presented in Figure S1).

Similar to the pristine MOF-303 structure, we also optimized the atomic coordinates of the MOF-303 structure at a loading of four water molecules per unit cell obtained from SCXRD measurements,[6] in the presence of the adsorbed water molecules, while keeping the unit cell parameters unchanged (Table S1). The resulting framework structure with the four water molecules per unit cell removed prior to the GEMC adsorption simulations, called E4D4, is the focus of our investigation of the adsorption behavior, but other structural variants (E4E4, D4D4, and E0D4) yield very similar isotherms (Figure 2). For the E4D4 structure, the initial uptake is very sharp with a loading of 4.88 water molecules per unit cell already at RH = 1.0% for the FF3-TIP4P model. The reason for this sharper uptake compared to the experimental data is an overestimation of Q_{st} by about 5 kJ mol^{-1} for the E4D4 structure and slightly larger amounts for the E4E4 and D4D4 structures (Figure 3). That is, the water binding in the primary site for the DFT-optimized structures is too favorable. It should be noted that the Q_{st} values obtained from the adsorption simulations are 25−30 kJ mol^{-1} smaller in magnitude than the 0 K binding energies at a loading of four water molecules per unit cell (Table S5). We surmise that thermal motion of the framework atoms (not allowed in our simulations using rigid framework structures) would further weaken the binding. Estimation from experimental data shows that Q_{st} becomes more favorable as the water loading is increased from two to four molecules per unit cell and less favorable as the loading is increased to six molecules (Figure 3), i.e., there is a cooperative effect as full loading of the primary site is attained. Since adsorption of the first four water molecules in the E4D4 and E0D4 structures with their already opened primary patch is not hampered by the need to distort the primary site, we do not observe the cooperative effect, i.e., there is likely negligible change in Q_{st} between the first and fourth water molecule. In agreement with the experimental data, the simulations for the E4D4 and E0D4 structures show that Q_{st} becomes less favorable as the loading increases beyond four molecules per unit cell.

Due to seeding of additional adsorption by the water molecules at the primary site, the inflection point for the FF3-TIP4P model in the E4D4 structure is shifted to lower RH compared to that for the E0D0 structure, and the former is an underprediction by a factor of 1.3 compared to the experimental data. The adsorption isotherm for the E4D4 structure also yields a more modest slope corresponding to an increase in the loading from four to eight water molecules that is also observed for the experimental isotherm. Simulations for the D4D4 structure (a

https://doi.org/10.1021/acs.jpcc.3c00354
J. Phys. Chem. C 2023, 127, 7837−7851

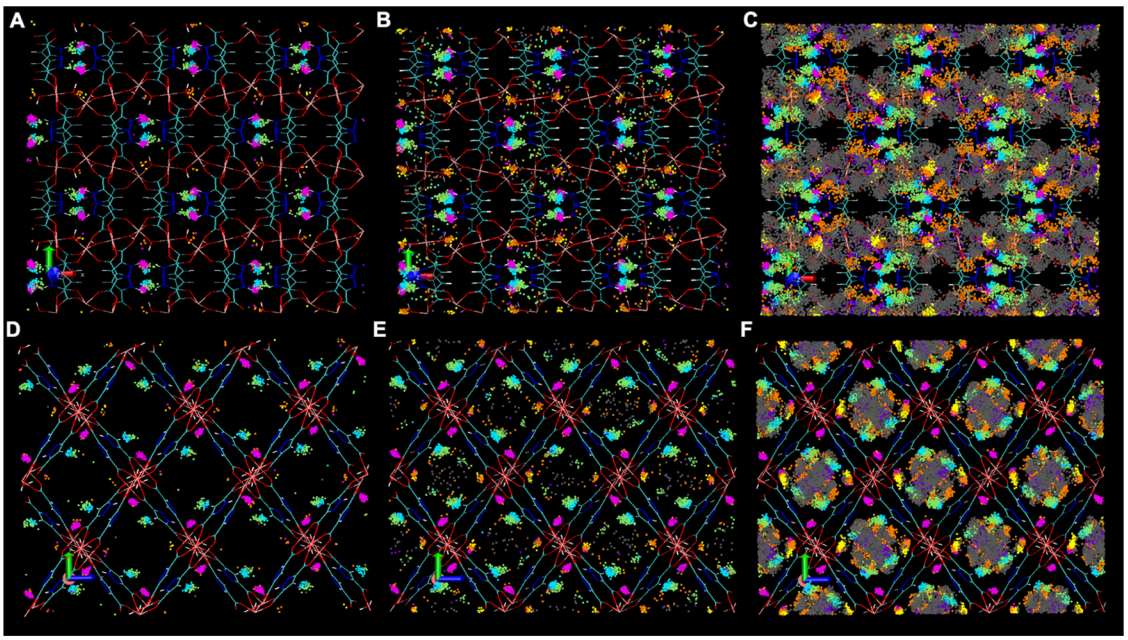

Figure 4. Spatial distribution of water molecules in the E4D4 MOF-303 structure at loadings of 4.88 (A, D), 7.56 (B, E), and 32.5 (C, F) molecules per unit cell obtained from GEMC simulations with the FF3-TIP4P model. Inclined views along the *c*-direction (top) and corresponding projections on the *b*−*c* plane (bottom) are shown. The MOF backbone is represented as lines, and the O-atom positions of the adsorbed water molecules (taken from 100 GEMC configurations) are shown as point clouds. Coloring of the water points according to the type of adsorption site and hydrogen-bond pattern: primary and secondary adsorption sites in magenta and cyan, respectively, other color codes are reported in Table 1.

full DFT optimization including the lattice parameters) result in a more favorable Q_{st} for the initial four molecules, but a much less favorable value as the loading exceeds four molecules per unit cell. Correspondingly, this part of the isotherm is too flat, and an intermediate state with eight water molecules is not observed. Using the experimental structure without optimization (E4E4) shifts the inflection point of the isotherm to the left and also does not produce the intermediate state with eight water molecules per unit cell, but yields better agreement for the saturation loading than the E4D4 structure. Furthermore, desorption simulations for the E4D4 structure yield negligible hysteresis in agreement with the experimental data. Overall, the combination of the E4D4 structure with the FF3-TIP4P model results in very good agreement with the experimental isotherm, as judged by the shape and location of the inflection point. Considering the significant deviations between binding energies predicted by FF3 and those obtained from PBE-D3 and MP2 electronic structure calculations and the sensitivity of the binding energy to small variation in the structure of the primary site (Table S5), good agreement with the experimental isotherm observed with the FF3-TIP4P model for the E4D4 structure (and to a slightly lesser extent for the E4E4 and D4D4 structures) may come as a surprise. However, for the remainder of the isotherm (RH > 2%), the water molecules tightly adsorbed at the primary site (see structural analysis presented later) become effectively part of the pore wall. The step of the water adsorption isotherm corresponds to water condensation in the pores of the MOF and it is mainly dominated by water−water interactions and the hydrophobicity of the organic pore walls (decorated by the water molecule in the primary site), which are well-described by the TIP4P water model and the TraPPE force field used here. Thus, the loading from about 5 to 40 water molecules per unit cell (the latter being the saturation loading) is not directly related to the adsorption strength for the first four water molecules (as long as these four water molecules remain in their locations).

The saturation loading obtained for the FF3-TIP4P model at RH = 92% is slightly affected by the structural variant used for the simulation with values of 39.8, 39.5, 37.7, 35.9, and 35.9 molecules per unit cell for E0D0, E0D4, E4E4, D4D4, and E4D4 structures, respectively. The variation in saturation loading is consistent with the differences in accessible pore volume (Table S2).

At this point, we briefly reconsider the performance of the different models for predicting the water uptake in the E4D4 structure (Figure S1). Consistent with the trend observed for the water binding energies in the E4D4 structure (Table S5), the initial water uptake is smallest for the FF1 model, followed by the FF2 and FF3 force fields. The shift in the location of the adsorption isotherm step is also consistent with the strength of the initial uptake, and the saturated water loading increases with decreasing repulsiveness of the H_{rod} atoms. Moreover, similar to FF1, a gradual increase in the initial water uptake with a much smaller slope in the Henry's law region is observed when DREIDING parameters for a nonpolar hydrogen atom are used for H_{rod} (Table S4, denoted the FF2-np parameter set). Clearly, the FF2 (using the polar H_{rod} parameters) and FF3 models are most suitable to describe the interactions of the primary water molecules with the framework. We note that the FF2 model gives a lower initial water uptake compared to FF3 and is in better agreement with the initial uptake of the experimental adsorption isotherm. However, the isotherm step for FF2 is shifted to higher RH by a factor of 1.3 compared to the experimental isotherm (while FF3 gives a similar shift but in the opposite direction) and the saturation loading is underpredicted to a slightly larger extent for FF2 compared to FF3. For comparison, we also computed the isotherm using the FF3 LJ parameters, but substituting all partial charges with those obtained with the DDEC6 scheme for the entire E4D4 structure.

https://doi.org/10.1021/acs.jpcc.3c00354
J. Phys. Chem. C 2023, 127, 7837−7851

Table 1. Color Code, Presence of Hydrogen Bonds with Different Framework Functionalities, and Occupancy Per Unit Cell at Representative RH Values for Different Water Adsorption Sites in the E4D4 Structure of MOF-303[a]

color	$N(H)_{linker}$	N_{linker}	O_{rod}	RH = 1.0%	RH = 5.1%	RH = 20.5%
Primary Patch on the Strongly Hydrophilic Region						
magenta	yes	yes	yes	3.95	3.96	4.09
orange	yes	yes	no	0.04	0.05	0.12
orange	yes	no	yes	0.05	0.32	1.64
orange	yes	no	no	0.00	0.05	0.80
orange	no	yes	yes	0.00	0.01	0.01
orange	no	yes	no	0.01	0.06	1.68
Secondary Patch on the Strongly Hydrophilic Region						
violet	yes	yes	yes	0.00	0.00	0.00
cyan	yes	yes	no	0.43	1.42	1.79
violet	yes	no	yes	0.00	0.00	0.00
violet	yes	no	no	0.02	0.07	1.11
violet	no	yes	yes	0.00	0.00	0.00
lime	no	yes	no	0.35	1.27	4.17
Other						
yellow	no	no	yes	0.02	0.11	1.65
gray	no	no	no	0.01	0.24	15.47

[a] $N(H)_{linker}$ and N_{linker} donors and acceptors are distinguished based on belonging to the primary or secondary patch ($d_{N(H)-N}$ = 3.9 and 3.5 Å, respectively). The first minima of the corresponding $X-O_{wat}$ radial distribution functions (where X = $N(H)_{linker}$, N_{linker}, O_{rod}, or O_{wat}) are used as the maximum distance to determine the presence of a hydrogen bond (Figure S2).

The DDEC6 charges for the polar functionalities of the linker, $N(H)_{linker}$ and N_{linker} (atom types N1, H2, and N2), which are part of the primary water adsorption sites, are smaller in magnitude compared to those assigned in the TraPPE-EH force field for pyrazole molecules (Table S3). Using the DDEC6 charges for the entire framework yields negligible water uptake for RH < 20% and a location of the isotherm step shifted by a factor of 2.5 toward higher RH (Figure S1).

To investigate the dependence on the water model, simulations were also carried out for the TIP4P/2005 model; the isotherm shape and saturation loading are very similar to the TIP4P data, but the inflection point for the TIP4P/2005 model is shifted to a lower RH and the Q_{st} is too favorable. Both observations can be attributed to the TIP4P/2005 model, yielding an overestimation of the heat of vaporization when a polarization correction is not applied. As noted previously by Grenev et al.[16] and Datar et al.,[19] expressing the isotherm as a function of absolute pressure (instead of RH) vastly increases the difference between the two water models (inset of Figure 2). Because the TIP4P/2005 model underpredicts the vapor pressure, its inflection point at 50 Pa is about a factor of 7 lower than the experimental data. In contrast, the TIP4P model slightly overpredicts the vapor pressure, and the inflection point is found at 410 Pa, a shift of about 10% compared to the experimental value.

We now focus on the analysis of the water siting and the water−MOF hydrogen-bond interactions. Figure 4 shows the spatial distribution of water molecules in the E4D4 MOF-303 structure for three characteristic loadings. At RH = 1.0%, just beyond the initial step, the loading is 4.88 molecules per unit cell for the FF3-TIP4P model. Upon adsorption at the primary adsorption site, the respective water molecule forms hydrogen bonds with both pyrazole functionalities ($N(H)_{linker}$, N_{linker}) and one of the bridging μ_2-OH groups (O_{rod}). The adsorbed molecules with this hydrogen-bond pattern are highlighted in magenta. The clouds of these magenta dots are highly localized (Figure 4) and represent 3.95 water molecules per unit cell at RH = 1.0% (Table 1). At finite temperature, we observe that another 0.10 water molecules per unit cell are adsorbed at the primary site, but do not form the complete set of hydrogen bonds (Table 1). Furthermore, at RH = 1.0%, an additional 0.80 molecules per unit cell are found adsorbed at the secondary adsorption site that are distributed nearly evenly over two different hydrogen-bond arrangements (shown as cyan and lime dots in Figure 4). It should be noted that in the E4D4 structure, the secondary site is too narrow to allow a water molecule to form hydrogen bonds with all three types of framework donor/acceptor sites. Prior periodic DFT calculations have indicated that the secondary site also widens upon adsorption of another four water molecules (for a total of eight) per unit cell,[6] but such a structure was not considered for the present simulations of the adsorption isotherms. Nevertheless, as the loading increases to 7.56 water molecules per unit cell at RH = 5.1% (just as the isotherm starts its steep rise, see Figure 2), we observe no increase in the loading of the primary site, an increase to 0.49 water molecules per unit cell for the remainder of the primary patch (shown as orange dots in Figure 4), and a large increase to 2.76 molecules per unit cell for the secondary patch; that is, 95% of the water molecules (7.21 out of 7.56) are adsorbed at the primary and secondary sites at this stage, which is in excellent agreement with the SCXRD data.[6] The water molecules adsorbed at the remainder of the primary patch mostly are lacking a hydrogen bond to the N_{linker} acceptor site and populate corners near the Al(μ_2-OH) units opposite to the primary adsorption site (see projection on the $b-c$ plane in Figure 4E). The cloud of water molecules adsorbed at the secondary patch is shifted away from the Al(μ_2-OH) units and is much more spread out than that for the primary patch.

At RH = 20.5%, the total loading is 32.5 water molecules per unit cell (about 90% of the full-saturation loading), but the loading at the primary sites increases to 4.09 molecules per unit cell, and the point cloud representing this site remains very well-localized. However, an additional 4.25 water molecules per unit cell are involved in at least one hydrogen bond to a donor/acceptor site on the primary patch. In addition, 7.07 water molecules per unit cell are involved in a least one hydrogen bond

https://doi.org/10.1021/acs.jpcc.3c00354
J. Phys. Chem. C 2023, 127, 7837−7851

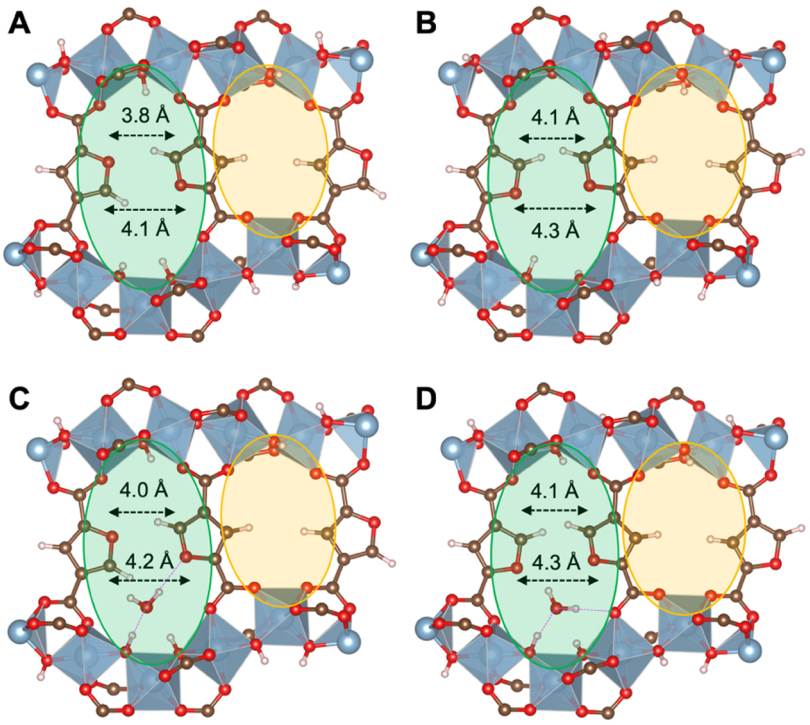

Figure 5. Illustrations of the pore walls for one asymmetric unit of pristine MOF-333 (for clarity, some of the surrounding atoms are shown). (A) E5D0 structure with *trans* arrangement of the 2,4-furandicarboxylate (FDC) linkers. (B) E5D0 structure with *cis* arrangement of the FDC linkers. (C) E5D4 structure with *trans* arrangements of the FDC linkers. (D) E5D4 structure with *cis* arrangement of the FDC linkers. The distances, $r_{O-O/C-O/C-C}$, between opposite FDC functionalities to each other are indicated. Structures are obtained from periodic DFT calculations using the experimental lattice parameters (with a loading of five water molecules per unit cell).[6] The more hydrophilic and less hydrophilic regions are shaded in green and yellow, respectively. Color code: Al, blue octahedra; O, red; C, brown; and H, light pink.

to the secondary patch. Only 1.65 water molecules form a hydrogen bond to the bridging μ_2-OH groups without an additional hydrogen bond to pyrazole functionalities (shown as yellow dots in Figure 4). Furthermore, at this loading, nearly half of the water molecules form hydrogen bonds exclusively with other water molecules and yield a continuous water filling of the cylindrical pore aligned with the crystallographic *a*-axis (illustrated by the gray cloud in Figure 4C,F).

For comparison, a similar analysis was also carried out for the adsorption isotherm obtained with the FF3-TIP4P model in the E0D0 structure (Figure S3 and Table S7) and with the FF3-TIP4P/2005 model in the E4D4 structure (Figure S4 and Table S8). When the primary adsorption site is in its narrow state (Figure 1B), as in the E0D0 structure, then the initial step is missing from the adsorption isotherm, and 0.49 molecules per unit cell is the highest loading observed for the FF3-TIP4P model before the major pore-filling step. Here, the loading at the primary patch is 0.21 molecules per unit cell, but there is no strong preference for a specific hydrogen-bond arrangement and the locations of the water molecules are spread out. The most significant clustering of the water locations is observed for water molecules that form hydrogen bonds with only the bridging μ_2-OH groups. The pore filling leads to large jumps in the number of water molecules hydrogen-bonded to the primary and secondary patches (8.4 and 5.7 molecules per unit cell, respectively), but the point clouds remain more spread out. The spatial distributions and hydrogen-bond patterns for the TIP4P and TIP4P/2005 water models at similar loadings (compare Figures 4 and S4) yield nearly indistinguishable data. Thus, when accounting for the differences in the saturated vapor pressures of these water models (i.e., comparing data at the same RH instead of absolute pressure), an extremely similar behavior is observed for isotherms and siting.

Adsorption in MOF-333. We further investigated the adsorption of water in MOF-333, a furan-based isoreticular analogue of MOF-303.[6] The Al rods in MOF-333 are connected by 2,4-furandicarboxylate (FDC) linkers. While the PZDC linkers in each hydrophilic region of MOF-303 were found to be predominantly oriented in the *trans* configuration, that is more stable relative to the *cis* configuration by 90 kJ mol^{-1} per unit cell (based on periodic DFT calculations), both *cis* and *trans* orientations of the FDC linkers (Figure 5) were found to coexist in MOF-333, as evidenced by the fractional occupancy determined for the O_{furan} in the SCXRD measurements and a comparable energetic stability computed for the two orientations: the *trans* configuration is favored by only 10.5 kJ mol^{-1} per unit cell relative to the *cis* orientation (Table S9). The reported crystal structure of MOF-333 contains five water molecules per unit cell that fractionally occupy eight sites, but the experimentally measured water loading in MOF-333 gradually increases up to four water molecules per unit cell followed by a single steep step in the isotherm (Figure 6).[6] We carried out geometry optimizations (without relaxing the unit cell parameters) to obtain two representative periodic structures, one each for *cis*-MOF-333 and *trans*-MOF-333, in the pristine form without any adsorbed water molecules and in the presence of four adsorbed water molecules per unit cell (Table S10).

These framework structures were used for GEMC simulations to predict the water adsorption isotherms. To this extent, the furan heterocycle is represented by the TraPPE force field, while the parameters for the Al(μ_2-OH) unit were transferred from MOF-303 (see Table S11 for the list of force-field parameters for

https://doi.org/10.1021/acs.jpcc.3c00354
J. Phys. Chem. C 2023, 127, 7837−7851

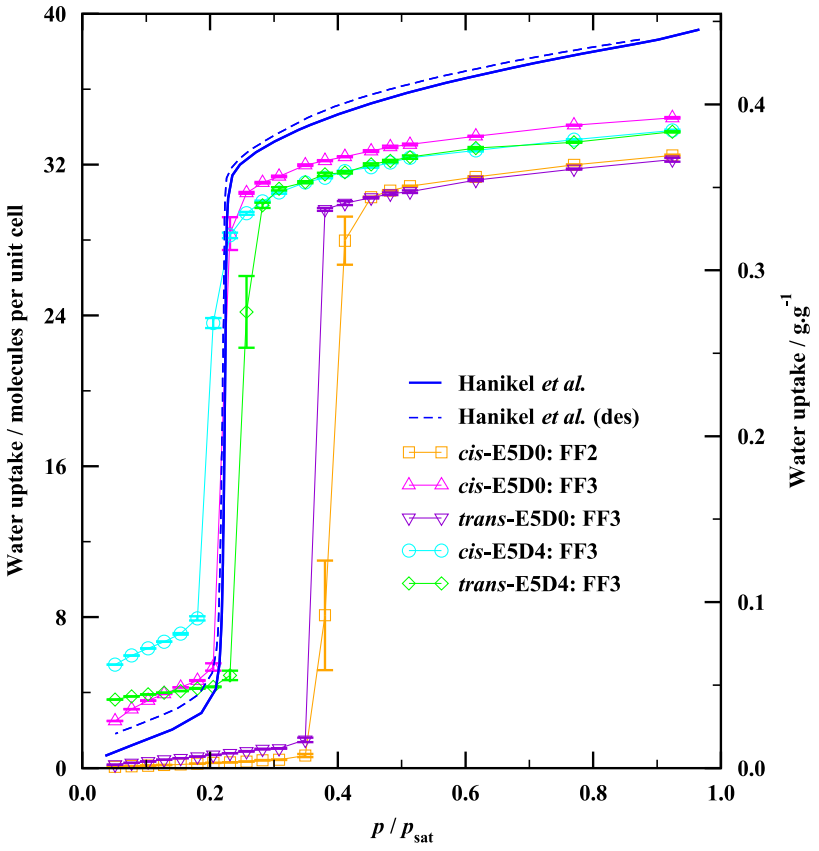

Figure 6. Comparison of simulated water sorption isotherms at T = 298 K in different structural variants of MOF-333 to the experimental data by Hanikel et al.[6] Simulations were carried out with the TIP4P water model, and only the adsorption branch is shown. Data for the pristine *cis*-MOF-333 structure optimized in the absence of adsorbed water molecules (D0) but using the experimental lattice parameters (E5) show the effects of variations in the Lennard-Jones parameter (FF2 versus FF3) used for the hydrogen atom of the Al(μ_2-OH) units. The remainder of the data illustrates the differences between *cis*- and *trans*-arrangements of MOF-333, as well as the impact of conducting the geometry optimization in the presence of four water molecules per unit cell (D4).

MOF-333). As mentioned above, the experimental isotherm of MOF-333 (Figure 6) exhibits only a single step at RH = 22% where the loading changes from 4 to 32 water molecules per unit cell and, by design to increase the working capacity, does not exhibit the initial step at very low RH caused by the strong adsorption at the primary site of MOF-303. As also observed for the simulated adsorption isotherms of MOF-303, replacing FF2 with FF3 (i.e., allowing for stronger hydrogen bonding to the μ_2-OH groups) shifts the step in the isotherm to lower RH, but this shift is more pronounced for MOF-333 (numerical data reported in Table S12). For the *cis*-E5D0 structure, the FF3-TIP4P model yields an isotherm that matches the location of the step perfectly and also exhibits the experimentally observed gradual increase in loading for RH < 20% as found experimentally. Considering the *trans*-E5D0 structure, the location of the step is shifted up in RH by a factor of 1.7, and the initial uptake before the step is greatly diminished. The opposing O groups in the FDC rings in the *cis*-arrangement allow for a significantly more favorable water adsorption site, but hydrogen bonding to the carboxylate oxygen is also observed (Figure 5). Utilizing MOF-333 structures optimized in the presence of four water molecules per unit cell (E5D4) results in more favorable adsorption sites and uptake of 5.48 and 3.63 water molecules per unit cell already at RH = 5.1% for the *cis*- and *trans*-arrangements of the linkers, respectively. This initial adsorption also leads to a downward shift of the major-step RH in the adsorption isotherm. Both *cis*-E5D4 and *trans*-E5D4 yield locations of the inflection point in good agreement (deviation of less than 10%), but the inflection points are shifted in opposite directions with their average falling very close to the experimental data.

Without knowledge of the experimental isotherms to select among the different structures of MOF-303 and MOF-333, it appears prudent to compute isotherms for a variety of structures that are energetically feasible. The energy difference of 90 kJ mol^{-1} per unit cell (based on periodic DFT calculations) between *trans* and *cis* forms for MOF-303 is prohibitive and only the *trans*-form needs to be considered, whereas the energy difference of 10 kJ mol^{-1} per unit cell between *trans* and *cis* forms for MOF-333 is sufficiently small that both should be used for subsequent simulations. With regard to inclusion of water molecules in the optimization of structures, our data point toward including such structures for the isotherm calculation when the presence of the water molecules yields significant changes in the positions of the framework atoms. For both MOF-303 and MOF-333, simulations for structures optimized with four water molecules per unit cell yield excellent predictions for the major step in the isotherms, but overestimate the loading at very low humidity (where the experiments show a more gradual uptake).

Data for the isosteric heat of adsorption in MOF-333 are shown in Figure 7. At a loading of four water molecules per unit cell, the experimental data yield Q_{st} = 50 kJ mol^{-1} for MOF-333, which is ~5 kJ mol^{-1} less favorable than Q_{st} for MOF-303 at the

https://doi.org/10.1021/acs.jpcc.3c00354
J. Phys. Chem. C 2023, 127, 7837−7851

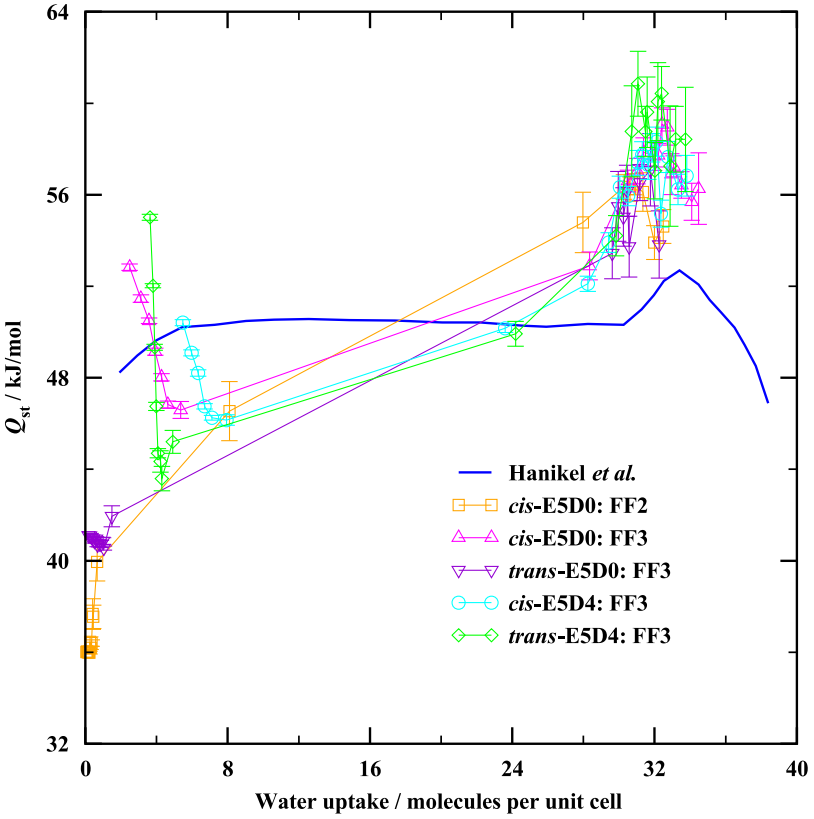

Figure 7. Comparison of the isosteric heat of adsorption Q_{st} at T = 298 K in different MOF-333 structural variants to the experimental data by Hanikel et al.[6] (estimated from data at multiple temperatures using the Clausius−Clapeyron equation). Simulations were carried out with the TIP4P water model, and only data for the adsorption branch is shown. Data for the pristine *cis*-MOF-333 structure optimized in the absence of adsorbed water molecules (D0) but using the experimental lattice parameters (E5) show the effects of variations in the Lennard-Jones parameter (FF2 versus FF3) used for the hydrogen atom of the Al(μ_2-OH) units. The remainder of the data illustrates the differences between the *cis*- and *trans*-form of MOF-333 and the impact of carrying out the geometry optimization in the presence of four water molecules per unit cell (D4).

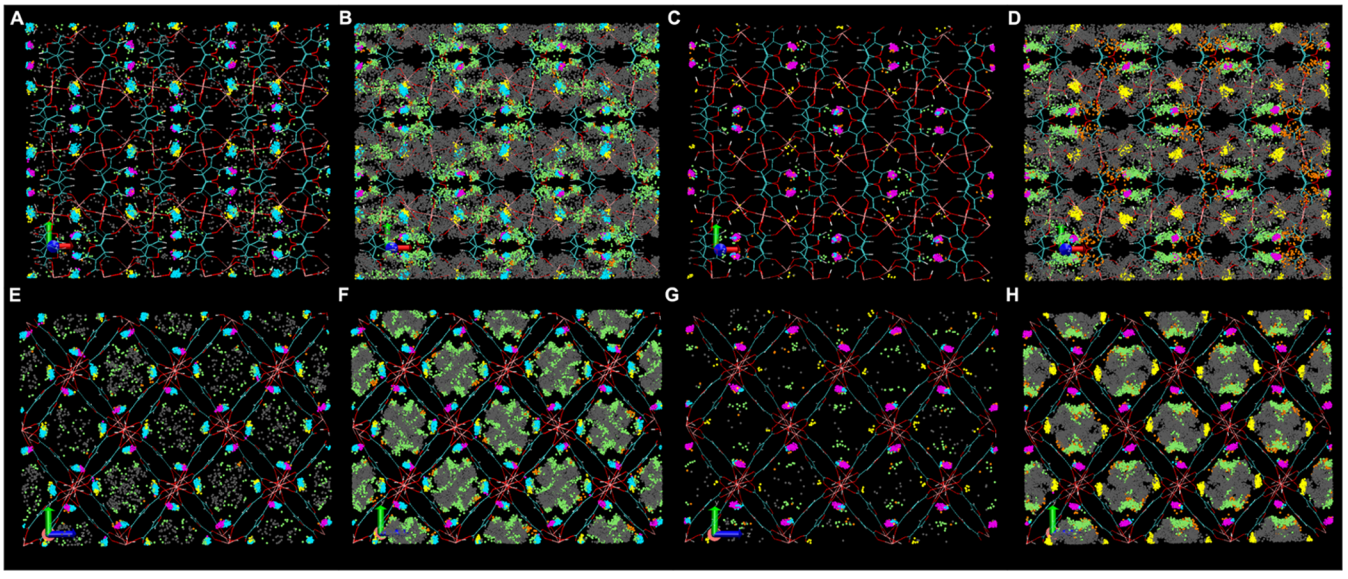

Figure 8. Spatial distribution of water molecules in the E5D4 *cis*-MOF-333 (A, B, E, F) and *trans*-MOF-333 (C, D, G, H) structures at loadings of 7.94 (A, E), 30.5 (B, F), 4.22 (C, G), and 30.7 (D, H) molecules per unit cell obtained from GEMC simulations with the FF3-TIP4P model. Inclined views along the *c*-direction (top) and corresponding projections on the *b*−*c* plane (bottom) are shown. The MOF backbone is represented as lines, and the O-atom positions of the adsorbed water molecules (taken from 100 GEMC configurations) are shown as point clouds. Colorings of the water points according to the types of adsorption site and hydrogen-bond pattern are reported in Table 2.

same loading. For MOF-333, however, there is no indication in the experimental data that Q_{st} becomes less favorable as the loading is increased from four to six molecules per unit cell. Similar to the data for MOF-303, the simulations for the E5D4

https://doi.org/10.1021/acs.jpcc.3c00354
J. Phys. Chem. C 2023, 127, 7837−7851

structures of cis- and trans-MOF-333 show that Q_{st} becomes less favorable as the loading increases from four to eight water molecules per unit cell. Somewhat surprisingly but in accordance with the adsorption isotherm, Q_{st} also becomes less favorable for the *cis*-E5D0 structure despite that the optimization was carried out in the absence of water molecules. A reason for this could be that the O−O distance between opposite FDC functionalities in this structure is already suitable for a water molecule to form multiple strong hydrogen bonds as indicated by the relatively small change in the structure (Figure 5B,D). Beyond the step in the adsorption isotherm, water−water interactions become more important and Q_{st} rises and reaches a maximum for about 32−34 water molecules per unit cell.

In the *cis*-MOF-333 structure, the arrangement of the furan linkers and nearby μ_2-OH groups allows for a strong binding site with multiple hydrogen-bond donor/acceptor groups. At a loading of eight molecules per unit cell in the *cis*-E5D4 structure (that is reached just before the large step in the isotherm), about 85% of the water molecules (6.7 water molecules per unit cell) are found adsorbed at the primary patch and form a well-localized point cloud (Figure 8 and Table 2). However, only

Table 2. Color Code, Presence of Hydrogen Bonds with Different Framework Functionalities, and Occupancy Per Unit Cell at Representative RH Values for Different Water Adsorption Sites in the E5D4 Structures of MOF-333[a]

color	O_{furan}	O_{rod}	RH = 18%	RH = 31%
cis-MOF-333: Primary Patch on the Strongly Hydrophilic Region				
magenta	two	yes	0.97	0.97
orange	two	no	0.01	0.28
cyan	one	yes	5.22	5.76
lime	one	no	0.51	5.16
cis-MOF-333: Other				
yellow	no	yes	0.31	0.60
gray	no	no	0.90	17.80
trans-MOF-333: Primary Patch on the Strongly Hydrophilic Region				
magenta	yes	yes	3.53	3.81
orange	yes	no	0.10	0.95
trans-MOF-333: Secondary Patch on the Strongly Hydrophilic Region				
cyan	yes	yes	0.25	0.07
lime	yes	no	0.13	3.93
trans-MOF-333: Other				
yellow	no	yes	0.09	3.02
gray	no	no	0.11	18.97

[a]For *cis*-MOF-333, the opposing O_{furan} acceptor sites result in the formation of only a primary adsorption patch but with the possibility for hydrogen-bonding to two O_{furan} functionalities, whereas primary and secondary patches are found for *trans*-MOF-333. The first minima of the corresponding X−O_{wat} radial distribution functions (where X = O_{furan} or O_{wat}) are used as maximum distance to determine the presence of a hydrogen bond (Figure S5).

12% of these molecules form hydrogen bonds to both O_{furan} acceptor sites, and the most favored pattern involves hydrogen bonds to one O_{furan} and one O_{rod} site. When the overall loading is increased to 30 molecules per unit cell (about 90% of the saturation loading), the loading at the primary patch increases to 12 molecules per unit cell with most of the increase being due to water molecules forming only a single hydrogen bond with an O_{furan} acceptor site, which results in a significant spread of the corresponding point cloud (lime-colored dots in Figure 8). The majority of the remaining water molecules form hydrogen bonds exclusively with other water molecules.

The *trans*-MOF-333 structure provides primary and secondary adsorption patches that are distinguished by the number and arrangement of the proximal μ_2-OH groups. Here, the loading reaches only a value of 4.2 molecules per unit cell before the major step in the isotherm. Most of these molecules (3.6 molecules per unit cell) are involved in hydrogen bonds to both one O_{furan} and one O_{rod} acceptor/donor site at the primary patch resulting in a well-localized point cloud. At near-saturation loading, the combined loading at the primary and secondary patches increases to 8.8 molecules per unit cell with 80% of this increase resulting from molecules forming a single hydrogen bond to the O_{furan} group at the secondary patch (lime-colored point cloud) but also some bonding exclusively to the O_{furan} group belonging to the primary patch (orange-colored point cloud). For *trans*-MOF-333, about 10% of the water molecules at saturation loading form a hydrogen bond exclusively to μ_2-OH groups of the framework (indicated by yellow point clouds).

CONCLUSIONS

To provide molecular-level information in the adsorption behavior of two high-performing Al-rod-based MOFs (MOF-303 and MOF-333) for water harvesting, isobaric−isothermal Gibbs ensemble Monte Carlo (GEMC) simulations have been performed to study water adsorption in multiple structural variants of MOF-303 and MOF-333 obtained from periodic DFT-based geometry optimizations and experimental diffraction studies. Given the importance of hydrogen bonding of water molecules to the bridging μ_2-OH of the Al rods, we find that caution is required to select suitable force-field parameters for the hydrogen atom of this hydroxyl group to allow for satisfactory binding energies compared to periodic DFT calculations and wave function calculations for cluster models. In contrast, the differences associated with the use of two different water models (i.e., nonpolarizable TIP4P and TIP4P/2005 models) are relatively small when the isotherms are reported as a function of relative humidity. The minor step in the adsorption isotherm for MOF-303 at very low humidity (RH < 5%) is only observed when utilizing a framework structure optimized in the presence of four water molecules per unit cell. On the other hand, the best representation of the initial water uptake in MOF-333 (RH < 20%) is obtained using a mixture of the *cis*- and *trans*-arrangements of the linkers that are optimized without any water molecule. This can be attributed to a larger structural deformation of MOF-303 than MOF-333 in the presence of water molecules loaded at the primary sites. The position and height of the major step in the isotherm, that is linked to the water-harvesting working capacity, are well reproduced using transferable force-field parameters for both MOF-303 and MOF-333.

This study highlights the importance of accounting for structural changes of the framework that are induced by the strong interactions with water molecules, particularly involving hydrogen-bond donor/acceptor sites of the MOF linkers and nodes. MOF structures at incremental water loadings are seldom reported experimentally, and the development of fully flexible force fields for MOFs can be challenging, especially when the MOF assumes different structures as a function of loading (versus harmonic oscillations around a mean structure that are well-described by a Hessian matrix). However, the sensitivity of the predicted guest molecule loading to the specific framework structure used is most pronounced when the guest molecule fits

https://doi.org/10.1021/acs.jpcc.3c00354
J. Phys. Chem. C 2023, 127, 7837−7851

tightly into the pore channels or into strong adsorption sites. Thus, we suggest a relatively inexpensive strategy that utilizes structures obtained by DFT optimization in the presence of only the strongly bound guest molecules to be a suitable surrogate for force-field-based simulations of entire adsorption isotherms (from the Henry's region to saturation). We surmise that this strategy may also yield satisfactory isotherms for other host−guest systems. We would like to advocate against attempts to switch between different rigid structures as the loading increases because discontinuous jumps in the isotherm will occur at points where a switch of structures is carried out.

Lastly, we would like to mention that this simulation strategy and the FF3 force-field parameters were recently successfully used to predict the water uptake in a novel linker-extended analogue of MOF-303, called MOF-LA2-1, where different linker configurations were considered to account for a partially disordered crystal structure.[55]

■ ASSOCIATED CONTENT

Supporting Information

The Supporting Information is available free of charge at https://pubs.acs.org/doi/10.1021/acs.jpcc.3c00354.

MOF-303-333-structures_cif.zip (ZIP)

MOF-303-333-isotherms_aif.zip (ZIP)

Lattice parameters and energies for different MOF structures; force-field parameters for the MOFs, binding energies for the first water molecule per asymmetric unit, numerical data for simulated water adsorption isotherms, figures showing the, radial distribution functions for the hydrogen-bond moieties, and additional spatial distribution plots; crystal structures of the rigid frameworks used for GEMC simulations are available as separate .cif files, and the adsorption isotherms are available as .aif files (PDF)

■ AUTHOR INFORMATION

Corresponding Authors

Laura Gagliardi − *Department of Chemistry, Pritzker School of Molecular Engineering, James Franck Institute, and Chicago Center for Theoretical Chemistry, University of Chicago, Chicago, Illinois 60637, United States;* orcid.org/0000-0001-5227-1396; Email: lgagliardi@uchicago.edu

J. Ilja Siepmann − *Department of Chemical Engineering and Material Science, University of Minnesota—Twin Cities, Minneapolis, Minnesota 55455, United States; Department of Chemistry and Chemical Theory Center, University of Minnesota—Twin Cities, Minneapolis, Minnesota 55455, United States;* orcid.org/0000-0003-2534-4507; Email: siepmann@umn.edu

Authors

Saumil Chheda − *Department of Chemical Engineering and Material Science, University of Minnesota—Twin Cities, Minneapolis, Minnesota 55455, United States; Department of Chemistry and Chemical Theory Center, University of Minnesota—Twin Cities, Minneapolis, Minnesota 55455, United States;* orcid.org/0000-0002-0989-5707

WooSeok Jeong − *Department of Chemistry and Chemical Theory Center, University of Minnesota—Twin Cities, Minneapolis, Minnesota 55455, United States*

Nikita Hanikel − *Department of Chemistry and Kavli Energy Nanoscience Institute, University of California, Berkeley, California 94720, United States;* orcid.org/0000-0002-3292-5070

Complete contact information is available at: https://pubs.acs.org/10.1021/acs.jpcc.3c00354

Notes

The authors declare no competing financial interest.

■ ACKNOWLEDGMENTS

This material is based upon work supported by the Defense Advanced Research Projects Agency (DARPA) under Contract No. HR0011-21-C-0020 (W.J., N.H., and L.G.) and Department of Energy, Office of Basic Energy Sciences, Division of Chemical Sciences, Geosciences and Biosciences under Award DE-FG02-17ER16362 (S.P.C. and J.I.S.). Any opinions, findings, and conclusions or recommendations expressed in this material are those of the author(s) and do not necessarily reflect the views of the DARPA. N.H. is grateful for the support through a Kavli ENSI Philomathia Graduate Student Fellowship and a Blavatnik Innovation Fellowship. The computational resources for this project were provided by the Minnesota Supercomputing Institute at the University of Minnesota and the Research Computing Center at the University of Chicago. Insightful discussions with Omar M. Yaghi are gratefully acknowledged. The authors also thank Hsiao-Feng Liu for performing the vapor−liquid equilibrium simulation to determine the saturated vapor pressure of the TIP4P water model at T = 298 K.

■ REFERENCES

(1) Mekonnen, M. M.; Hoekstra, A. Y. Four Billion People Facing Severe Water Scarcity. *Sci. Adv.* **2016**, *2*, No. e1500323.

(2) Kim, H.; Yang, S.; Rao, S. R.; Narayanan, S.; Kapustin, E. A.; Furukawa, H.; Umans, A. S.; Yaghi, O. M.; Wang, E. N. Water Harvesting from Air with Metal-Organic Frameworks Powered by Natural Sunlight. *Science* **2017**, *356*, 430−434.

(3) Kim, H.; Rao, S. R.; Kapustin, E. A.; Zhao, L.; Yang, S.; Yaghi, O. M.; Wang, E. N. Adsorption-Based Atmospheric Water Harvesting Device for Arid Climates. *Nat. Commun.* **2018**, *9*, No. 1191.

(4) Hanikel, N.; Prévot, M. S.; Fathieh, F.; Kapustin, E. A.; Lyu, H.; Wang, H.; Diercks, N. J.; Glover, T. G.; Yaghi, O. M. Rapid Cycling and Exceptional Yield in a Metal-Organic Framework Water Harvester. *ACS Cent. Sci.* **2019**, *5*, 1699−1706.

(5) Zhou, X.; Lu, H.; Zhao, F.; Yu, G. Atmospheric Water Harvesting: A Review of Material and Structural Designs. *ACS Mater. Lett.* **2020**, *2*, 671−684.

(6) Hanikel, N.; Pei, X.; Chheda, S.; Lyu, H.; Jeong, W.; Sauer, J.; Gagliardi, L.; Yaghi, O. M. Evolution of Water Structures in Metal-Organic Frameworks for Improved Atmospheric Water Harvesting. *Science* **2021**, *374*, 454−459.

(7) Ng, E.-P.; Mintova, S. Nanoporous Materials with Enhanced Hydrophilicity and High Water Sorption Capacity. *Microporous Mesoporous Mater.* **2008**, *114*, 1−26.

(8) Hanikel, N.; Prévot, M. S.; Yaghi, O. M. MOF Water Harvesters. *Nat. Nanotechnol.* **2020**, *15*, 348−355.

(9) Zhu, Z.; Xu, H.; Jiang, J.; Wu, H.; Wu, P. Hydrophobic Nanosized All-Silica Beta Zeolite: Efficient Synthesis and Adsorption Application. *ACS Appl. Mater. Interfaces* **2017**, *9*, 27273−27283.

(10) Sauer, J. Ab Initio Calculations for Molecule−Surface Interactions with Chemical Accuracy. *Acc. Chem. Res.* **2019**, *52*, 3502−3510.

(11) Fetisov, E. O.; Shah, M. S.; Long, J. R.; Tsapatsis, M.; Siepmann, J. I. First Principles Monte Carlo Simulations of Unary and Binary Adsorption: CO_2, N_2, and H_2O in Mg-MOF-74. *Chem. Commun.* **2018**, *54*, 10816−10819.

(12) Bai, P.; Neurock, M.; Siepmann, J. I. First-Principles Grand-Canonical Simulations of Water Adsorption in Proton-Exchanged Zeolites. *J. Phys. Chem. C* **2021**, *125*, 6090−6098.
(13) McGrath, M. J.; Siepmann, J. I.; Kuo, I.-F. W.; Mundy, C. J. Vapor−Liquid Equilibria of Water from First Principles: Comparison of Density Functionals and Basis Sets. *Mol. Phys.* **2006**, *104*, 3619−3626.
(14) Mileo, P. G. M.; Ho Cho, K.; Park, J.; Devautour-Vinot, S.; Chang, J.-S.; Maurin, G. Unraveling the Water Adsorption Mechanism in the Mesoporous MIL-100(Fe) Metal−Organic Framework. *J. Phys. Chem. C* **2019**, *123*, 23014−23025.
(15) Jajko, G.; Gutiérrez-Sevillano, J. J.; Sławek, A.; Szufla, M.; Kozyra, P.; Matoga, D.; Makowski, W.; Calero, S. Water Adsorption in Ideal and Defective UiO-66 Structures. *Microporous Mesoporous Mater.* **2022**, *330*, No. 111555.
(16) Grenev, I. V.; Shubin, A. A.; Solovyeva, M. V.; Gordeeva, L. G. The Impact of Framework Flexibility and Defects on the Water Adsorption in CAU-10-H. *Phys. Chem. Chem. Phys.* **2021**, *23*, 21329−21337.
(17) Fei, S.; Alizadeh, A.; Hsu, W.-L.; Delaunay, J.-J.; Daiguji, H. Analysis of the Water Adsorption Mechanism in Metal−Organic Framework MIL-101(Cr) by Molecular Simulations. *J. Phys. Chem. C* **2021**, *125*, 26755−26769.
(18) Datar, A.; Witman, M.; Lin, L.-C. Improving Computational Assessment of Porous Materials for Water Adsorption Applications via Flat Histogram Methods. *J. Phys. Chem. C* **2021**, *125*, 4253−4266.
(19) Datar, A.; Witman, M.; Lin, L. Monte Carlo Simulations for Water Adsorption in Porous Materials: Best Practices and New Insights. *AIChE J.* **2021**, *67*, No. e17447.
(20) Zhao, X. S.; Siepmann, J. I.; Xu, W.; Kiang, Y.-H.; Sheth, A. R.; Karaborni, S. Exploring the Formation of Multiple Layer Hydrates for a Complex Pharmaceutical Compound. *J. Phys. Chem. B* **2009**, *113*, 5929−5937.
(21) Bai, P.; Tsapatsis, M.; Siepmann, J. I. Multicomponent Adsorption of Alcohols onto Silicalite-1 from Aqueous Solution: Isotherms, Structural Analysis, and Assessment of Ideal Adsorbed Solution Theory. *Langmuir* **2012**, *28*, 15566−15576.
(22) Rappe, A. K.; Casewit, C. J.; Colwell, K. S.; Goddard, W. A.; Skiff, W. M. UFF, a Full Periodic Table Force Field for Molecular Mechanics and Molecular Dynamics Simulations. *J. Am. Chem. Soc.* **1992**, *114*, 10024−10035.
(23) Mayo, S. L.; Olafson, B. D.; Goddard, W. A. DREIDING: A Generic Force Field for Molecular Simulations. *J. Phys. Chem. A* **1990**, *94*, 8897−8909.
(24) Ghosh, P.; Colón, Y. J.; Snurr, R. Q. Water Adsorption in UiO-66: The Importance of Defects. *Chem. Commun.* **2014**, *50*, 11329−11331.
(25) Choi, J.; Lin, L.-C.; Grossman, J. C. Role of Structural Defects in the Water Adsorption Properties of MOF-801. *J. Phys. Chem. C* **2018**, *122*, 5545−5552.
(26) Berendsen, H. J. C.; Grigera, J. R.; Straatsma, T. P. The Missing Term in Effective Pair Potentials. *J. Phys. Chem. B* **1987**, *91*, 6269−6271.
(27) Jorgensen, W. L.; Chandrasekhar, J.; Madura, J. D.; Impey, R. W.; Klein, M. L. Comparison of Simple Potential Functions for Simulating Liquid Water. *J. Chem. Phys.* **1983**, *79*, 926−935.
(28) Abascal, J. L. F.; Vega, C. A General Purpose Model for the Condensed Phases of Water: TIP4P/2005. *J. Chem. Phys.* **2005**, *123*, No. 234505.
(29) Dubbeldam, D.; Torres-Knoop, A.; Walton, K. S. On the Inner Workings of Monte Carlo Codes. *Mol. Simul.* **2013**, *39*, 1253−1292.
(30) Panagiotopoulos, A. Z. Direct Determination of Phase Coexistence Properties of Fluids by Monte Carlo Simulation in a New Ensemble. *Mol. Phys.* **1987**, *61*, 813−826.
(31) Panagiotopoulos, A. Z.; Quirke, N.; Stapleton, M.; Tildesley, D. J. Phase Equilibria by Simulation in the Gibbs Ensemble: Alternative Derivation, Generalization and Application to Mixture and Membrane Equilibria. *Mol. Phys.* **1988**, *63*, 527−545.
(32) Vega, C.; Abascal, J. L. F. Simulating Water with Rigid Non-Polarizable Models: A General Perspective. *Phys. Chem. Chem. Phys.* **2011**, *13*, 19663.
(33) Xue, B.; Harwood, D. B.; Chen, J. L.; Siepmann, J. I. Monte Carlo Simulations of Fluid Phase Equilibria and Interfacial Properties for Water/Alkane Mixtures: An Assessment of Nonpolarizable Water Models and of Departures from the Lorentz−Berthelot Combining Rules. *J. Chem. Eng. Data* **2018**, *63*, 4256−4268.
(34) Rai, N.; Siepmann, J. I. Transferable Potentials for Phase Equilibria. 9. Explicit Hydrogen Description of Benzene and Five-Membered and Six-Membered Heterocyclic Aromatic Compounds. *J. Phys. Chem. B* **2007**, *111*, 10790−10799.
(35) Kresse, G.; Hafner, J. *Ab Initio* Molecular Dynamics for Liquid Metals. *Phys. Rev. B* **1993**, *47*, 558−561.
(36) Kresse, G.; Furthmüller, J. Efficiency of Ab-Initio Total Energy Calculations for Metals and Semiconductors Using a Plane-Wave Basis Set. *Comput. Mater. Sci.* **1996**, *6*, 15−50.
(37) Kresse, G.; Furthmüller, J. Efficient Iterative Schemes for *Ab Initio* Total-Energy Calculations Using a Plane-Wave Basis Set. *Phys. Rev. B* **1996**, *54*, 11169−11186.
(38) Perdew, J. P.; Burke, K.; Ernzerhof, M. Generalized Gradient Approximation Made Simple. *Phys. Rev. Lett.* **1996**, *77*, 3865−3868.
(39) Grimme, S.; Ehrlich, S.; Goerigk, L. Effect of the Damping Function in Dispersion Corrected Density Functional Theory. *J. Comput. Chem.* **2011**, *32*, 1456−1465.
(40) Frisch, M. J.; Head-Gordon, M.; Pople, J. A. A Direct MP2 Gradient Method. *Chem. Phys. Lett.* **1990**, *166*, 275−280.
(41) Frisch, M. J.; Head-Gordon, M.; Pople, J. A. Semi-Direct Algorithms for the MP2 Energy and Gradient. *Chem. Phys. Lett.* **1990**, *166*, 281−289.
(42) Frisch, M. J.; Trucks, G. W.; Schlegel, H. B.; Scuseria, G. E.; Robb, M. A.; Cheeseman, J. R.; Scalmani, G.; Barone, V.; Petersson, G. A.; Nakatsuji, H.; Li, X.; Caricato, M.; Marenich, A. V.; Bloino, J.; Janesko, B. G.; Gomperts, R.; Mennucci, B.; Hratchian, H. P.; Ortiz, J. V.; Izmaylov, A. F.; Sonnenberg, J. L.; Williams-Young, D.; Ding, F.; Lipparini, F.; Egidi, F.; Goings, J.; Peng, B.; Petrone, A.; Henderson, T.; Ranasinghe, D.; Zakrzewski, V. G.; Gao, J.; Rega, N.; Zheng, G.; Liang, W.; Hada, M.; Ehara, M.; Toyota, K.; Fukuda, R.; Hasegawa, J.; Ishida, M.; Nakajima, T.; Honda, Y.; Kitao, O.; Nakai, H.; Vreven, T.; Throssell, K.; Montgomery, J. A., Jr.; Peralta, J. E.; Ogliaro, F.; Bearpark, M. J.; Heyd, J. J.; Brothers, E. N.; Kudin, K. N.; Staroverov, V. N.; Keith, T. A.; Kobayashi, R.; Normand, J.; Raghavachari, K.; Rendell, A. P.; Burant, J. C.; Iyengar, S. S.; Tomasi, J.; Cossi, M.; Millam, J. M.; Klene, M.; Adamo, C.; Cammi, R.; Ochterski, J. W.; Martin, R. L.; Morokuma, K.; Farkas, O.; Foresman, J. B.; Fox, D. J. *Gaussian 16*, revision C.01; Gaussian, Inc.: Wallingford CT, 2016.
(43) Dunning, T. H. Gaussian Basis Sets for Use in Correlated Molecular Calculations. I. The Atoms Boron through Neon and Hydrogen. *J. Chem. Phys.* **1989**, *90*, 1007−1023.
(44) Woon, D. E.; Dunning, T. H. Gaussian Basis Sets for Use in Correlated Molecular Calculations. III. The Atoms Aluminum through Argon. *J. Chem. Phys.* **1993**, *98*, 1358−1371.
(45) Siepmann, J. I.; Martin, M. G.; Chen, B.; Wick, C.; Stubbs, J. M.; Potoff, J. J.; Eggimann, B. L.; McGrath, M. J.; Zhao, X. S.; Anderson, K. E.; Rafferty, J. L.; Rai, N.; Maerzke, K. A.; Keasler, S. J.; Bai, P.; Fetisov, E. O.; Shah, M. S.; Chen, Q. P.; DeJaco, R. F.; Chen, J. L.; Xue, B.; Bunner, C.; Sun, Y. Z. S.; Josephson, T. R. *Monte Carlo for Complex Chemical Systems−Minnesota*, version 20.2; University of Minnesota: Minneapolis, MN, 2020.
(46) Manz, T. A.; Limas, N. G. Introducing DDEC6 Atomic Population Analysis: Part 1. Charge Partitioning Theory and Methodology. *RSC Adv.* **2016**, *6*, 47771−47801.
(47) Chen, J. L.; Xue, B.; Mahesh, K.; Siepmann, J. I. Molecular Simulations Probing the Thermophysical Properties of Homogeneously Stretched and Bubbly Water Systems. *J. Chem. Eng. Data* **2019**, *64*, 3755−3771.
(48) Bridgeman, O. C.; Aldrich, E. W. Vapor Pressure Tables for Water. *J. Heat Transfer* **1964**, *86*, 279−286.

https://doi.org/10.1021/acs.jpcc.3c00354
J. Phys. Chem. C 2023, 127, 7837−7851

(49) Karavias, F.; Myers, A. L. Isosteric Heats of Multicomponent Adsorption: Thermodynamics and Computer Simulations. *Langmuir* **1991**, *7*, 3118−3126.
(50) Chen, B.; Potoff, J. J.; Siepmann, J. I. Monte Carlo Calculations for Alcohols and Their Mixtures with Alkanes. Transferable Potentials for Phase Equilibria. 5. United-Atom Description of Primary, Secondary, and Tertiary Alcohols. *J. Phys. Chem. B* **2001**, *105*, 3093−3104.
(51) Stubbs, J. M.; Potoff, J. J.; Siepmann, J. I. Transferable Potentials for Phase Equilibria. 6. United-Atom Description for Ethers, Glycols, Ketones, and Aldehydes. *J. Phys. Chem. B* **2004**, *108*, 17596−17605.
(52) Jorgensen, W. L.; Maxwell, D. S.; Tirado-Rives, J. Development and Testing of the OPLS All-Atom Force Field on Conformational Energetics and Properties of Organic Liquids. *J. Am. Chem. Soc.* **1996**, *118*, 11225−11236.
(53) Rai, N.; Siepmann, J. I. Transferable Potentials for Phase Equilibria. 10. Explicit-Hydrogen Description of Substituted Benzenes and Polycyclic Aromatic Compounds. *J. Phys. Chem. B* **2013**, *117*, 273−288.
(54) Wardzala, J. J.; Ruffley, J. P.; Goodenough, I.; Schmidt, A. M.; Shukla, P. B.; Wei, X.; Bagusetty, A.; De Souza, M.; Das, P.; Thompson, D. J.; Karwacki, C. J.; Wilmer, C. E.; Borguet, E.; Rosi, N. L.; Johnson, J. K. Modeling of Diffusion of Acetone in UiO-66. *J. Phys. Chem. C* **2020**, *124*, 28469−28478.
(55) Hanikel, N.; Kurandina, D.; Chheda, S.; Zheng, Z.; Rong, R.; Neumann, S. E.; Sauer, J.; Siepmann, J. I.; Gagliardi, L.; Yaghi, O. M. MOF Linker Extension Strategy for Enhanced Atmospheric Water Harvesting. *ACS Cent. Sci.* **2023**, *9*, 551−557.

https://doi.org/10.1021/acs.jpcc.3c00354
J. Phys. Chem. C 2023, 127, 7837−7851